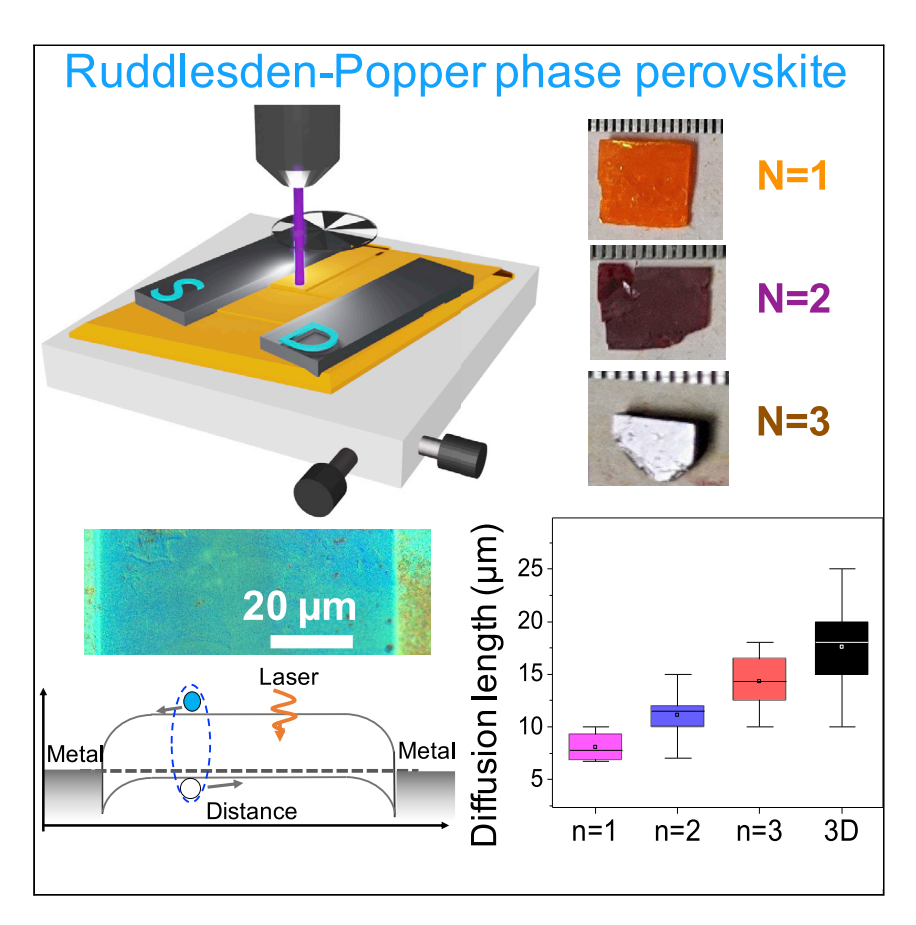




Article

Long carrier diffusion length in twodimensional lead halide perovskite single crystals



Free carrier transport dominates in 2D perovskite single-crystal devices.

Shreetu Shrestha, Xinxin Li, Hsinhan Tsai, ..., Sergei Tretiak, Xuedan Ma, Wanyi Nie

wanyi@lanl.gov

Highlights

This paper elucidates the carrier transport properties in 2D perovskites

Long diffusion lengths are observed

Free carriers dominate the charge transport

Comprehensive mechanism discussions are provided



Shrestha et al., Chem 8, 1–14 April 14, 2022 Published by Elsevier Inc. https://doi.org/10.1016/j.chempr.2022.01.008

Chem



Article

Long carrier diffusion length in two-dimensional lead halide perovskite single crystals

Shreetu Shrestha,¹ Xinxin Li,^{2,9} Hsinhan Tsai,¹ Cheng-Hung Hou,³ Hsin-Hsiang Huang,^{4,5} Dibyajyoti Ghosh,^{1,6,7} Jing-Jong Shyue,³ Leeyih Wang,^{4,5,8} Sergei Tretiak,^{1,6,7} Xuedan Ma,^{2,9} and Wanyi Nie^{1,10,*}

SUMMARY

Ruddlesden-Popper (RP) perovskites are two-dimensional semiconductors for high-performance optoelectronic devices. In this work, we report a long in-plane carrier diffusion length in 2D RP perovskite single crystals probed by scanning photocurrent microscopy. Carrier diffusion lengths of 7-14 μm are observed when the number of Pbl₆⁻² octahedra between organic spacers increases from 1 to 3. Using detailed light intensity and electric-field-dependent photocurrent measurements, we attribute the observed long diffusion length to the dominating dissociated free carrier transport. This is further validated by time-resolved photoluminescence measurements, where the decay lifetime increases in the presence of an electric field. From our experiments, we conclude that the in-plane transport in RP perovskites is efficient because of the partial free carrier generation, which overcomes strong excitonic effects. Our results suggest that semiconducting devices fabricated from RP perovskite single crystals can be as efficient as their 3D counterparts.

INTRODUCTION

Two-dimensional (2D) Ruddlesden-Popper (RP) phase perovskites are layered semiconducting materials that have promise for a wide range of optoelectronic devices and have demonstrated record-breaking performances. A typical RP structure consists of inorganic metal-halide octahedral layers (MX₆) intercalated between bulky organic spacer cations, described by the general formula (A')₂(A)_{n-1}M_nX_{3n+1}, where A' is the bulky spacer cation. Here, A is a monovalent organic cation, M is a divalent metal cation, X is a halide, and n refers to the number of octahedral layers between spacer cations. Owing to the hydrophobic nature of the bulky cations, steric hindrances, and passivation effects, ¹⁻³ 2D perovskites exhibit improved material and device stability compared with their 3D counterparts, making them technologically relevant for optoelectronic device applications, such as photovoltaics⁴ and lightemitting diodes. ⁴ Moreover, 2D perovskite single-crystal devices have been recently integrated into highly efficient photo and X-ray detectors, featuring significantly suppressed ion migration under high electrical field stressing. ⁵⁻⁷

The organic spacers have larger band gaps and lower dielectric constants than the inorganic layers, resulting in interesting photophysical properties due to the interplay of quantum and dielectric confinement.^{8,9} Large exciton-binding energies in the range of hundreds of meV have been reported, and the photo-generated carriers are believed to be dominated by strongly bound excitons at room temperature.^{10,11} As the number of PbI₆⁻² octahedral layers between organic spacers (n)

The bigger picture

Ruddlesden-Popper (RP) layered perovskites are promising materials for stable photovoltaics and light-emitting diodes. This work elucidates an unusual long carrier diffusion length in RP perovskite single crystals by the scanning photocurrent microscopy technique. Detailed device characteristics suggest that the carrier transport in the RP perovskite single crystals is dominated by free carrier diffusion. The carrier dissociation mechanisms are discussed, and a carrier trapping-detrapping mechanism can explain the experimental observations.

Our work suggests that the carrier transport in the RP perovskites can be as efficient as that in their 3D counterparts. Because of these superior properties, semiconducting devices made from RP perovskites can be both efficient and environmentally stable.





increases, the exciton-binding energy gradually decreases and eventually falls below room temperature thermal energy for n = ∞ or 3D perovskites. ¹⁰ This potentially differentiates the charge transport in 2D perovskites from 3D perovskites, where the transport is dominated by free carriers at room temperature. The quantum and dielectric confinement effects in 2D perovskites make them ideal candidates for light emission applications in which rapid and efficient charge recombination is desirable. On the other hand, it is reported that excitons in 2D perovskites can be dissociated into free carriers assisted by localized states at the layer edges, ^{12–16} traps, ^{17,18} or lower n-numbered phase, ¹⁹ when multiple n-numbered RP phases are present. Therefore, a thorough understanding of exciton dynamics, dissociation, and free carrier transport is the key guide to the material design for high-performance devices.

Studies on exciton transport in 2D perovskites conducted so far were carried out predominately by optical probing methods, such as time-resolved photoluminescence (TRPL) imaging 17,18,20-22 and transient absorption microscopy, 23 where exciton diffusion is mapped by tracking emission or absorption in time and space domains. The exciton diffusion length of 2D perovskites in the range of a few nanometers to hundreds of nanometers has been reported using these techniques. ^{20,22,23} On the other hand, Zhao et al. used PL imaging and TRPL to demonstrate that long-distance exciton transport up to 2–5 μm in 2D perovskite single crystals could be enabled by trap-assisted exciton dissociation. ¹⁷ Similarly, Seitz et al. further suggest that there is a distinct distribution of trap states that are responsible for the observed long-distance transport. 18 Although optical probing techniques do provide valuable insight into the intrinsic properties of the 2D perovskites, processes that neither emit fluorescence nor absorb photons can go undetected. For example, charges that are thermally emitted from shallow trap states can contribute to photocurrent. However, information on such trapping and detrapping processes is often inaccessible using optical techniques. Moreover, precise measurement of carrier transport behavior in a device, where interfaces and internal electric fields are present, is still lacking.

In this paper, we present direct experimental evidence of long-distance charge diffusion lengths in the 7–14 μ m range in 2D perovskite single-crystal devices probed by scanning photocurrent microscopy (SPCM). Specifically, by mapping the locally excited photocurrent across a Schottky barrier formed between the perovskite/ metal interface, we obtained a photocurrent decay profile from which the exciton diffusion length could be extracted. A systematic increase in the diffusion length was observed as n increased from 1 to 3. Markedly, the diffusion lengths in 2D perovskites were in the same order of magnitude as those of their 3D counterparts. To understand the long diffusion length, we conducted detailed SPCM studies as a function of electric field and laser intensity, from which we attribute the long diffusion length to predominately free charge carrier transport. This was further validated by time-resolved photoluminescence measurement on the same devices, where the presence of an electric field extends the recombination lifetime. We attribute an efficient free carrier generation to the exciton dissociation assisted by trap states. Our study complements the optical spectroscopy measurements reported in the literature and provides a comprehensive understanding and analysis of the origin of long exciton transport in 2D perovskites in a device configuration.

RESULTS

We focus on the 2D perovskite single crystals having a composition of $(C_4H_9NH_3)_2(CH_3NH_3)_{n-1}Pb_nI_{3n+1}$ (or $(BA)_2(MA)_{n-1}Pb_nI_{3n+1}$), where n ranges from

¹Center for Integrated Nanotechnologies, Los Alamos National Laboratory, Los Alamos, NM 87545, USA

²Center for Nanoscale Materials, Argonne National Laboratory, Lemont, IL 60439, USA

³Research Center for Applied Sciences, Academia Sinica, Taipei 11529, Taiwan

⁴Center for Condensed Matter Sciences, National Taiwan University, No. 1, Sec. 4, Roosevelt Rd., Taipei 10617, Taiwan

⁵Department of Material Science and Engineering, National Taiwan University, No. 1, Sec. 4, Roosevelt Rd., Taipei 10617, Taiwan

⁶Theoretical Division, Los Alamos National Laboratory, Los Alamos, NM 87545, USA

⁷Center for Nonlinear Studies, Los Alamos National Laboratory, Los Alamos, NM 87545, USA

⁸Center of Atomic Initiative for New Materials, National Taiwan University, Taipei 10617, Taiwan

⁹Consortium for Advanced Science and Engineering, University of Chicago, Chicago, Illinois 60637, United States

¹⁰Lead contact

*Correspondence: wanyi@lanl.gov https://doi.org/10.1016/j.chempr.2022.01.008





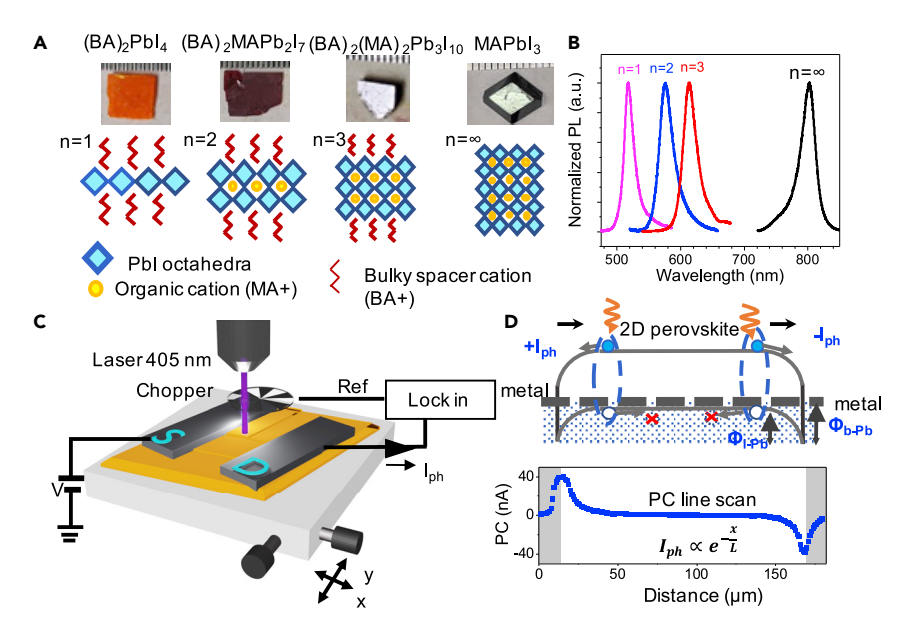


Figure 1. 2D Ruddlesden-Popper phase layered perovskite structures and the experimental setup

- (A) Pictures of different perovskite single crystals and their schematic crystal structures.
- (B) Photoluminescence obtained from perovskite single crystals.
- (C) Schematic illustration of the scanning photocurrent microscopy (SPCM) setup. Lateral devices are mounted on a piezoelectric stage, and voltage (V) is applied on the source electrode (S), while the drain electrode (D) is grounded.
- (D) Energy diagram (top) with band bending at the perovskite/metal interface with corresponding photocurrent line scan (bottom). Electron is shown as a filled circle, hole is shown as an empty circle, and a blue dotted line represents a bound exciton. E_f, $l_{\rm ph}$, q, $V_{\rm b}$, $\Phi_{\rm b}$, x, and L refer to the Fermi level, photocurrent, elementary charge, built-in potential, barrier height at metal/perovskite junction, distance, and carrier diffusion length, respectively.

1 to 3. The 2D crystals are synthesized using the cooling method reported in the literature 24,25 and typically have lateral sizes between 2 and 10 mm and thicknesses of 0.1–1 mm (Figure 1A). For comparison, we also study the 3D analog (n = ∞), i.e., MAPbl₃ single crystals grown by the inverse temperature crystallization method. Figure 1B shows the photoluminescence spectra of n = 1, 2, and 3 and 3D single crystals with peaks at 518, 577, 613, and 803 nm, respectively. As the n value increases, the photoluminescence peak gradually red shifts toward higher wavelengths corresponding to the respective band gaps of 2.39, 2.15, 2.02, and 1.54 eV, which is in good agreement with values reported in the literature. Sharp grazing incidence X-ray diffraction peaks from (0k0) planes (Figure S1), and X-ray photoelectron spectroscopy characterization (Figures S2 and S3) confirmed the 2D crystal structure and phase purity with the Pbl₆ octahedral layer parallel to the substrate.

Scanning photocurrent microscopy characterization

The SPCM technique (Figure 1C) has been implemented in a wide variety of semi-conducting materials, such as perovskites, ^{27,28} transition-metal dichalcogenides, ²⁹ carbon nanotubes, ³⁰ and quantum dot thin films. ³¹ We employ SPCM to map the photocurrent distribution in the lateral 2D perovskite single-crystal devices to study charge transport. Here, charge carriers are locally excited by a focused laser, and as the device is moved along x and y directions with respect to the laser, the corresponding photocurrent is recorded at each position to form a photocurrent map,





as illustrated in Figure 1C. We focus a 405 nm continuous wave laser (1–2 μm spot size) on a 2D perovskite device with lateral contacts and scan the device along x-and y-directions in 1 μm increments while measuring the photocurrent as a function of laser position. To improve the signal-to-noise ratio of the photocurrent signal, we use an optical chopper to modulate the laser at 20 Hz and then record the photocurrent with a lock-in amplifier at the same frequency. This setup ensures that only the current induced by the laser modulated at the same frequency is recorded to minimize the possible contributions from other factors, such as dark noise and ambient signals.

SPCM measurements take advantage of the electrostatic barrier (or Schottky barrier) at a metal/semiconductor junction. As shown in Figure 1D, when a downward band bending is present near the perovskite/metal interface, electrons can be collected via the internal electric field at both the drain and source interfaces. A typical photocurrent profile (Figure 1D, bottom) features the photocurrent maxima (minima) appearing near the drain (source) metal/perovskite interface as a result of electron collection. The laser locally photoexcites free and bonded carriers (excitons), and when the laser is close to the metal electrodes, free carriers and excitons diffuse into the depletion region at the interface where collection occurs. If the interface built-in potential is large, then it can dissociate bound excitons into free carriers. For downward band bending, electrons are extracted resulting in a photocurrent signal while holes are blocked. As the laser moves away from the metal electrodes, fewer charge carriers and excitons can diffuse to the depletion, region resulting in a photocurrent decay. Provided that the electrodes form a Schottky barrier, carrier diffusion limits the photocurrent, and thus, the carrier diffusion length can be extracted from the photocurrent decay using the formula:

$$I_{ph} \propto \exp\left(-\frac{x}{L}\right)$$
 (Equation 1)

where I_{ph} is the photocurrent, x is the distance away from the electrode, and L is the diffusion length.³²

Carrier diffusion length extracted by SPCM

To fabricate lateral devices, we cleaved the 2D crystals with scotch tape to expose a fresh surface and deposit metal electrodes with a channel width of 160 μ m, as shown in Figure 2A. To build a Schottky barrier, Pb was selected as the electrode for SPCM due to its low work-function (4.2 eV). In our previous work, we have demonstrated that low work-function metal (Pb) forms a Schottky barrier, whereas high work-function metal (Au) forms an ohmic barrier with MAPbI₃.²⁷ The dark and light current-voltage (I-V) characteristics shown in Figure 2B establish that this is also the case for n = 3 2D perovskite. An S-shaped curve is obtained when we illuminate n = 3 lateral device with the laser focused on the middle of the channel (position 2), and asymmetric curves are obtained when we move the laser near the electrodes (positions 1 and 3). This can be explained by considering the two Pb/ perovskite interfaces as two Schottky junctions or diodes connected back to back (inset in Figure 2A).³³ The energy band diagram derived from the ultraviolet photoelectron spectroscopy (UPS) results in Figures 2C and S4 demonstrates that the work-function of 2D perovskites is higher than that of Pb. The work-function increases with decreasing n from 4.98 eV (for n = 3) to 5.46 eV (for n = 1). This difference in the metal and 2D perovskite work-function gives rise to an electrostatic barrier, which explains the observed diode I-V characteristics. The photocurrent is two orders of magnitude higher than the dark current (Figure S5), indicating that the crystals are of good quality.





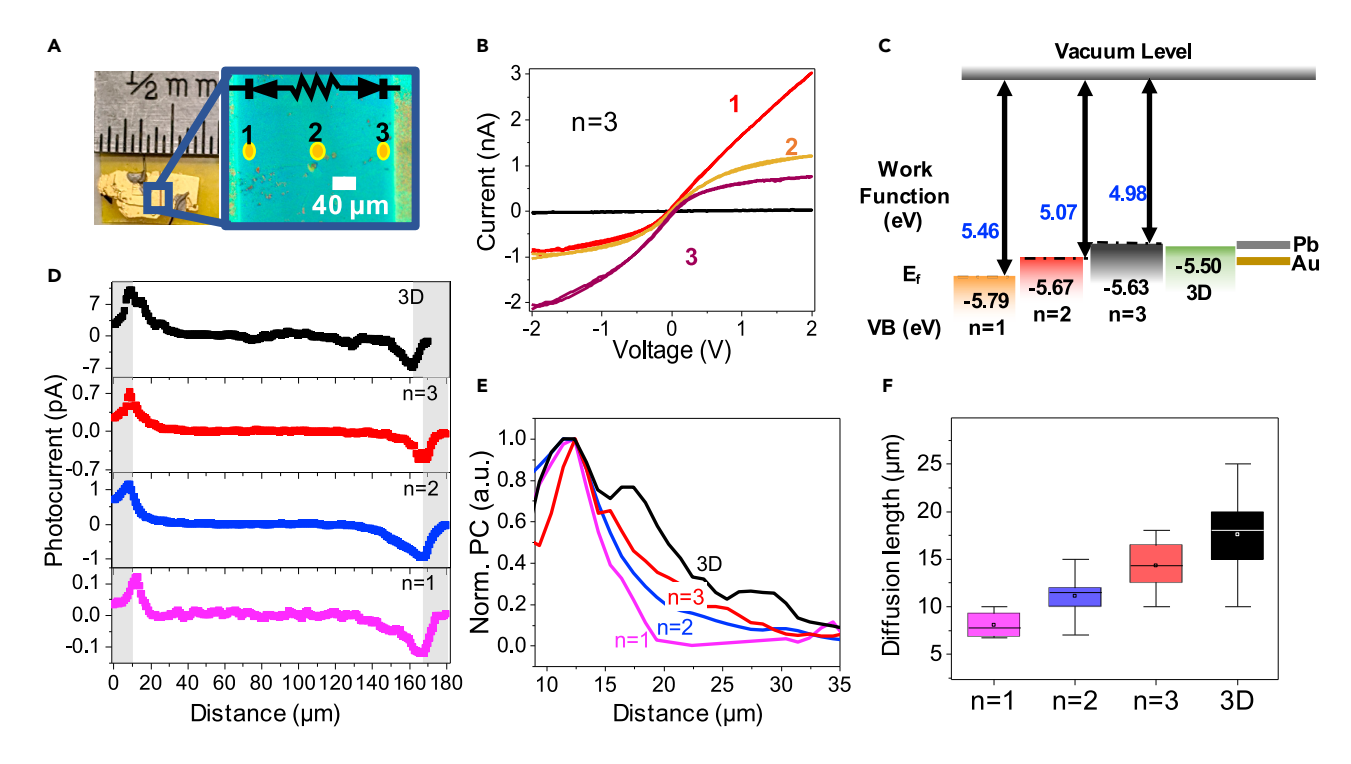


Figure 2. Scanning photocurrent measurement characterization

(A) Picture of a 2D perovskite lateral device with metal contacts and zoomed-in optical microscopy image of the perovskite channel between the source (left) and drain (right) electrode showing positions 1, 2, and 3. A schematic of two diodes at the two electrodes connected back to back is also shown.

(B) I-V measurements of n = 3 device in the dark (black) and with 405 nm laser illumination at positions 1, 2, and 3.

- (C) Schematic of the energy band diagram derived from UPS measurements.
- (D and E) (D) Photocurrent line scans for 3D, n = 3, n = 2, and n = 1 and (E) normalized photocurrent line scans comparison.
- (F) Boxplot of diffusion lengths extracted from the decay of the photocurrent line scans. The box is determined by the 25th and 75th percentiles, and the dot inside the box represents the mean value.

The photocurrent line scans for 3D, n = 3, 2, and 1 hybrid perovskites with the position of Pb contacts shaded in gray are shown in Figure 2D. All line scans show a positive and a negative peak near the source (left) and the drain (right) electrode, respectively, as expected and explained earlier by Schottky barriers with downward energy band bending (Figure 1D). The photocurrent peak for 3D MAPbl $_3$ is about 10 pA, which decreases by two orders of magnitude for n = 1. Note that the photocurrent amplitudes for n = 2 and n = 3 are similar and slightly vary from batch to batch. We analyze the normalized photocurrent decay profiles plotted in Figure 2E. Here, a faster decay is observed for lower n 2D perovskites, and a relatively long decay is present in the device made from 3D materials. The diffusion lengths derived from the photocurrent decay using the Equation 1 and plotted in Figure 2F for n = 1, 2, 3, and ∞ , are 7 ± 2 , 11 ± 4 , 14 ± 4 , and 18 ± 8 μ m, respectively. There is a clear trend that the diffusion length decreases with a concomitant decrease in n.

Time-resolved spectroscopy techniques can also be used to measure the diffusion length by probing the photon emission or absorption to map exciton population in space and time. The main difference is that in SPCM, the diffusion length is extracted from the decay in photocurrent, whereas in transient spectroscopy techniques, it is extracted from the decay in photoluminescence or absorption. The values obtained from both techniques should be comparable. However, there are several processes that do not emit or absorb photons, which cannot be detected



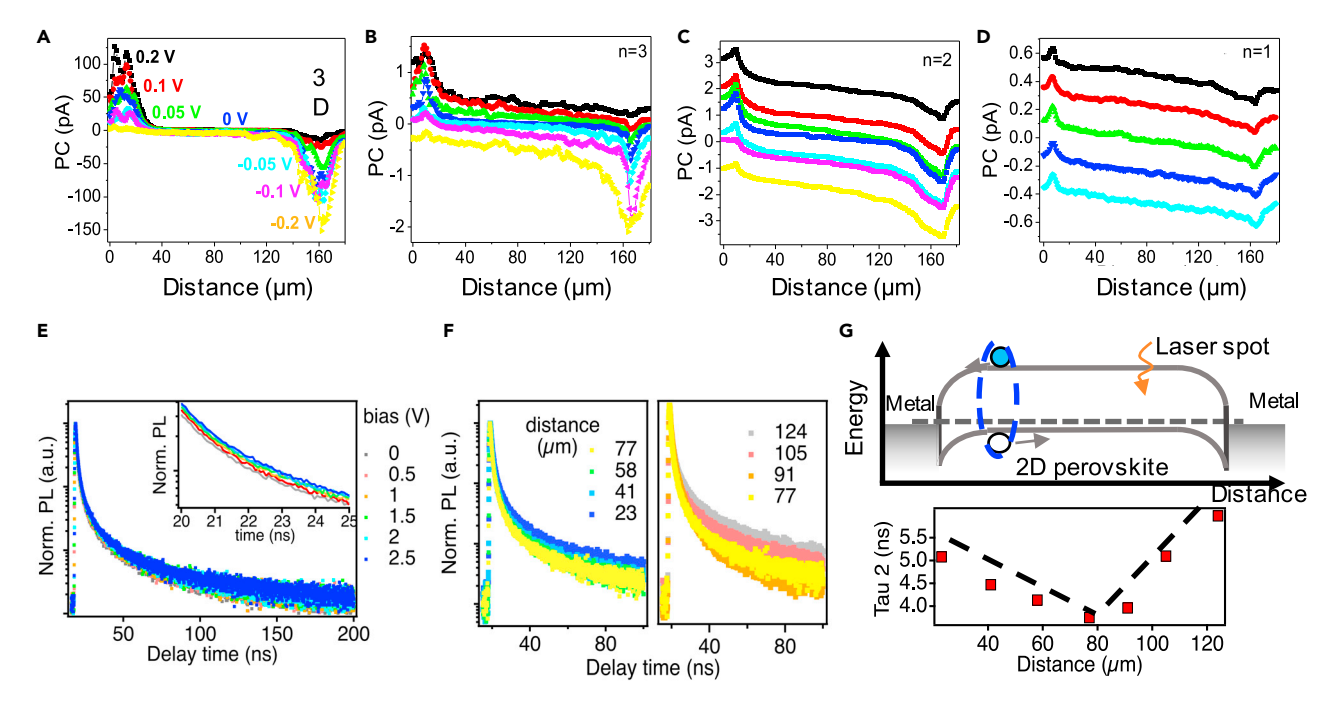


Figure 3. Electric-field dependence

(A–D) Electric-field dependence of photocurrent line scans of (A), 3D (B) n = 3, (C) n = 2, and (D) n = 1 perovskite single-crystal devices. (E and F) Time-resolved PL (E) with different electric fields and (F) when probed at various distances from the drain/left electrode (the total channel width is 160 μ m).

(G) Extracted TRPL lifetime as a function of channel position along with the schematic illustration of the lateral device used in SPCM.

by optical probes, resulting in an underestimation of the diffusion length. For instance, charges that are thermally emitted from the trap states can also contribute to the photocurrent. The carrier trapping-detrapping process, proposed in our study, can also result in a detectable electrical signal.

We attribute both the smaller photocurrent magnitude and the shorter diffusion length in lower *n*-numbered 2D perovskite devices to the larger exciton-binding energy. Moreover, the interface built-in potential, which is estimated to be 1.26–0.78 V from the difference in metal and perovskite work-functions obtained from UPS measurements, is much larger than the exciton-binding energy. Therefore, excitons that reach the interface will very likely dissociate due to the built-in potential, and the limiting process is the excitons reaching the interface. We also notice that the diffusion lengths of the 2D perovskites are generally of the same order of magnitude, approaching that of the 3D crystal. Markedly, these values are much longer than those reported in the literature, ^{20,22,23} which will be discussed in detail in the rest of this paper.

Electric-field dependence

To rationalize the observed long diffusion length in 2D perovskites, we further performed electric-field-dependent SPCM complemented by field-dependent time-resolved photoluminescence spectroscopy to probe the nature of the photo-excited carriers (Figure 3). In literature, the carriers have been attributed to dominating Wannier excitons in n = 1 and to free carriers in n = ∞ at room temperature, whereas for n values in between these two extreme cases, the picture is less clear. ^{10,16,34,35} The excitons as charge-neutral particles are not responsive to the externally applied field,





whereas the free charge carriers are sensitive to the electric field.³⁶ Moreover, although the built-in potential at the interface is sufficient to dissociate excitons, the externally applied field in the middle of the channel is not sufficient to separate excitons. Figure 3A shows the line profile for the 3D MAPbl₃ singlecrystal device when an external field is applied. When a positive bias is applied to the source, the photocurrent at the source is increased, with a concomitant decrease at the drain. Since the photo-generated carriers in 3D MAPbl₃ are dominated by free carriers, a field-dependent charge collection due to carrier drift is expected. Figure 3D shows the photocurrent line profiles measured for n = 1. In sharp contrast, the photocurrent profile does not change when the external field is applied. We attribute this to the dominance of strongly bound excitonic carriers in the n = 1 crystal and, as expected, their transport does not show noticeable electric-field dependence. Interestingly, when n increases, as shown in Figures 3A-3D, the photocurrent profile starts to show field dependence. Markedly, the profile for n = 3 becomes similar to that of the 3D perovskite device, which suggests a noticeable growth of the free charge carriers with increasing n. Note that due to the lower photoconductivity of n = 1 samples, we use 500 W/cm² laser intensity while we use $50 \text{ W/cm}^2 \text{ for 3D}$, n = 3, and n = 2. (Photocurrent profile for n = 1 at 50 W/cm^2 shown in Figure S7.)

To further understand the nature of observed carrier transport, we performed timeresolved PL on a typical RP single-crystal device (n = 3) with an applied bias, as shown in Figure 3E. In the curve, a rapid decay (<1 ns) is first observed at the early time followed by a longer decay (>1 ns). Typically, the fast decay is attributed to the trap-assisted recombination, and the longer component is assigned to bimolecular recombination.^{37,38} This is further validated by a power-dependent TRPL (Figure S8), where the lifetime of the longer component, which is inversely proportional to the carrier density, shows a clear pump fluence dependence. When we apply an electric field to the device, the long component of the TRPL decay corresponding to the free carrier recombination becomes longer (e.g., inset in Figure 3E that shows a zoomedin section). Because the interface depletion width does not extend beyond 1 μ m, our measurement (at least 20 µm away from the contact) is dominated by the externally applied field. Due to the presence of an electric field, the free (or dissociated) electrons and holes get pulled in opposite directions, resulting in a lower probability of their collision and radiative recombination. This is equivalent to a reduction in the carrier densities, which would further reduce the bimolecular recombination rate. In addition, we compare the TRPL curves when moving the photoexcitation from the middle of the channel toward the perovskite/metal interface in Figures 3F and 3G. The lifetime fitting methodology is described in Figures S8-S11. As depicted in Figure 3F, when the distance between the metal interface and the laser spot decreases, the generated carriers can reach the depletion region to be collected by the electrode, resulting in an extended lifetime for the slow decay component. By contrast, when the laser is in the middle of the channel, fewer carriers can diffuse to the contact, and a shorter PL lifetime is observed. In summary, both the fielddependent and distance-dependent TRPL results support the field-dependent SPCM results, where free carrier transport/recombination plays a vital role in n = 32D perovskites.

Light intensity dependence

To gain more insights into the origin of long diffusion lengths observed in the 2D crystals, we further investigate the light-intensity-dependent photocurrent for a typical 2D device. Figure 4A shows the normalized photocurrent profiles from n = 3 2D perovskite devices at different laser intensities ranging from 1.2 to





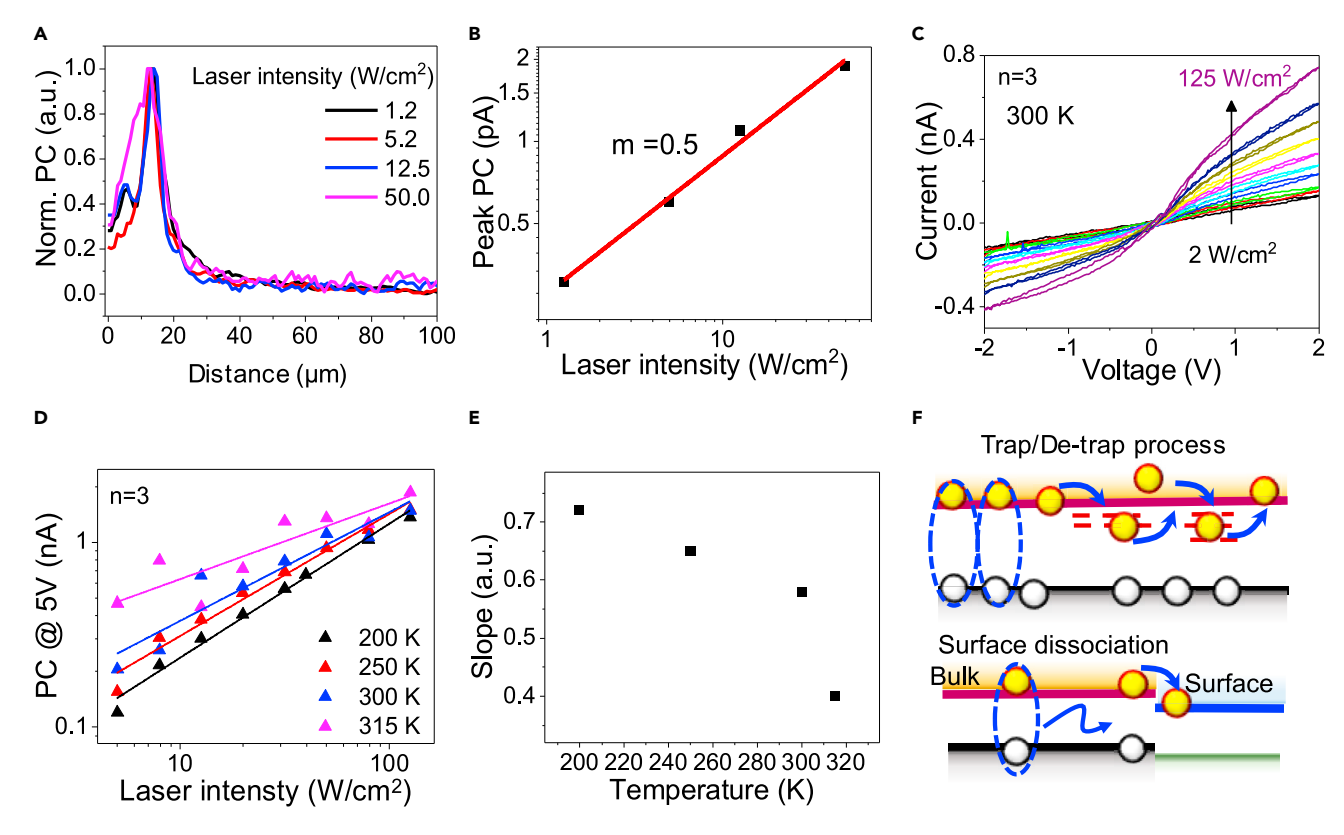


Figure 4. Laser intensity and tempearture dependence

- (A) normalized photocurrent profiles of n=3 at different laser intensities.
- (B) Peak photocurrent as a function of laser intensity extracted from (A).
- (C) $\emph{I-V}$ curve as a function of light intensity at room temperature.
- (D) Photocurrent at different laser intensities and temperatures.
- (E) Slope of fit from (D) as a function of temperature.
- (F) Schematics illustrating the two dissociation mechanisms: trap-assisted carrier dissociation and surface-state-mediated dissociation.

 $50~{\rm W/cm^2}$. Here, the laser power was kept low to avoid perturbation of the internal field generated near the interface. The photocurrent decay profile remains the same, whereas the peak photocurrent increases with laser intensity (Figure 4B). The photocurrent amplitude versus intensity curve follows a power-law relation $I_{ph} \propto P^{0.5}$. The power dependence deviates from a linear relation when approaching higher laser power. This behavior has been interpreted by the recombination loss via bimolecular processes, which is dependent on the carrier density. This value also agrees well with values reported in the literature for 2D perovskites in the high laser intensity range where the bimolecular recombination is significant. 39,40

Next, we measured the *I-V* characteristics as a function of laser intensity and temperature when the laser spot is fixed in the middle of the channel to understand the power dependence of photocurrents at low temperatures. Because we target to measure the crystals' resistivity, high work-function Au electrodes are employed that form ohmic contacts with the crystal. Figure 4C shows the *I-V* curves obtained under different laser intensities at 300 K, and Figure 4D plots the photocurrent at 5 V as a function of laser intensity at a temperature ranging from 200 to 315 K. At each temperature, the data are fitted to the power-law relation (I^{α}). Figure 4E extracts the α value and plots them as a function of temperature. Clearly, lowering the temperature increases α from 0.4 to 0.7. This suggests that current collection limited by the





bimolecular recombination is suppressed at a lower temperature, which results in a higher value of α . It also indicates that the free carrier generation is thermally activated.

DISCUSSION

From SPCM measurements, we find that the charge carrier diffusion length increases from 7 to 14 μm when n increases from 1 to 3. Meanwhile, the diffusion length observed in n = 3 single crystal (14 μm) is close to that of the 3D single crystal (25 μm). In addition, a significant electrical field dependence is observed in both photocurrent profile and time-resolved PL lifetime for higher n 2D single-crystal device. In particular, n = 3 2D RP perovskite exhibits significant field dependence, similar to that of the 3D device. By contrast, carrier transport behavior for lower n RP perovskite devices becomes independent of external electric fields. The photocurrent collection efficiency and carrier lifetime in the higher n RP perovskites (n = 3) can be improved by applying an external electric field. These observations suggest that a significant portion of the photo-generated carriers become free charge carriers that contribute to the observed long diffusion length and the radiative recombination shown in Figure 2.

After photoexcitation, both (1) dissociation of excitons and (2) exciton migration are involved. We have presented a study for 2D perovskites with different n numbers (number of inorganic layers between organic spacers). 2D perovskites with a lower n number have higher exciton-binding energy and are more likely to be bound at room temperature. In our measurement, the photocurrent signal is generated by free carrier collection and recombination in the outer circuits. The excitons will first diffuse to the depletion region, which extends only a few hundred nanometers from the metal interface, and then get split due to the interface built-in potential. From UPS measurements, we have obtained the work-function, which indicates that the interface built-in potential (i.e., the difference between the work-functions of the metal and semiconductor) is much larger than the exciton-binding energy. Therefore, excitons that can reach the interface are highly likely to be dissociated at the interface, and the limiting process is the excitons reaching the interface.

However, we do not expect the exciton generated far from the electrodes (i.e., 15 μm) to reach the depletion region given the short lifetime of a typical exciton recombination. According to our results, the measured diffusion lengths in higher n number perovskites (about 15 μm) are much longer than the depletion width (a few hundred nm). Therefore, we believe that before the exciton can migrate to the interface, the dissociation already happens. As proposed in the paper and supported by literature discussion, we think the excitons can be trapped and de-trapped by lower energy states, and they are more likely to be dissociated into free carriers. These free carriers diffuse to the metal interface and get extracted, resulting in a photocurrent. Therefore, although both processes (1) and (2) are present, we show that in lower n-numbered perovskite excitons diffusion is dominant, whereas in the higher n-numbered perovskites with free charge carrier diffusion is dominant. This leads to the conclusion that trap-assisted exciton dissociation followed by an efficient free charge migration could underpin the long diffusion lengths we observe in high n perovskites.

Previous studies by Blancon et al. suggested that excitons can dissociate at room temperature only in layered lead iodide perovskites with $n \ge 20.10$ Thus, we discuss other factors, such as the trap-assisted exciton dissociation process and





surface-states-mediated dissociation (Figure 4F), to understand its possible involvement in free charge carrier generation and transport. From our powerdependent photocurrent measurements at various temperatures, we conclude that, although the nature of carriers in 2D perovskites (exciton dominated) is expected to be vastly different from that in 3D perovskites (free charge carrier dominated), the transport in higher n 2D perovskites is still dominated by free charge carriers. Charge transport is suppressed by lowering the temperature, suggesting that the free carrier generation is a thermally activated process. This can be interpreted as lower bimolecular recombination because of the suppression of shallow trap-assisted thermal dissociation at lower temperatures. This is consistent with literature reports on "edge state" 12,15 or trap-assisted dissociation. These "edge states" are formed due to the surface relaxation leading to rotating octahedral for n = 3 as suggested by experimental observations 12 and detailed by extensive quantum chemical simulations. 41 In particular, calculations have shown that ingap edge states lead to spatial localization of carriers and separation of the electron and hole wavefunctions, thus facilitating the exciton dissociation and generation of free carriers. This exciton dissociation at surface-localized sub-gap electronic states has also been confirmed by subsequent experimental studies. 14 By contrast, for n = 1 and n = 2, the octahedral motions do not lead to localization, and electrons and holes remain spatially delocalized over the entire inorganic layer, providing improved spatial overlap between their wavefunctions. Apart from the trapping-detrapping mechanism, we further consider an alternative mechanism, which is the exciton dissociation via the surface states. As suggested in the literature, 12,15 the surface states (or edge states) can also dissociate the bonded exciton. Such states can either be lower energy states, such as shallow traps, or a type-II heterostructure near the surface that cascade one type and block another type of carrier (Figure 4F). Previous reports have attributed the interface heterostructure to the different n-numbered phase impurities in the single crystals' surfaces, forming a cascading energy alignment.⁴²

Moreover, distinct distribution of trap states in 2D perovskites has been associated with long exciton diffusion. ¹⁸ Using time-resolved PL microscopy on 2D perovskites, Seitz et al. find an initial fast exciton diffusion followed by a sub-diffusive regime to which they attribute the presence of traps. ²⁰ Zhao et al. have also reported trapmediated long-distance carrier transport in phenethylamine (PEA)-based 2D perovskites. ¹⁷

Similarly, photon recycling, which is the iterative reabsorption of emission from radiatively recombining excitons, could also be present. However, the consensus in recent literature is that the contribution of photon recycling to transport in perovskites is negligible, especially for low-illumination conditions. ^{17,23,43–45}

In conclusion, we investigate the charge transport behaviors in 2D RP perovskite single-crystal devices by combining optical and electrical measurements. From SPCM measurements, we obtain direct experimental evidence for long in-plane charge carrier diffusion length with a systematic increase in the diffusion length as n increases from 1 (7 \pm 2 μ m) to 3 (14 \pm 4 μ m). These values are in the same order of magnitude and approach to that for 3D perovskites (18 \pm 8 μ m). Supported by the electric field and laser intensity dependence studies, we attribute these long diffusion lengths to predominantly free charge carrier transport, which is generated predominantly by trap-assisted exciton dissociation. This is further validated by time-resolved photoluminescence measurements where the carrier lifetime increases in the presence of an electric field. Our study provides a comprehensive understanding of exciton/free





carrier transport in 2D perovskites in the presence of interfaces and electric fields, which is a key parameter for further device optimization.

2D perovskites are more stable under heat, moisture, and electric field. In recent years, 2D perovskite thin film growth techniques have been successfully implemented to control the orientation of the films so that charge transport occurs inplane, resulting in high-performance devices. Our results corroborate these findings by directly demonstrating that in-plane carrier transport and charge collection in single-crystal 2D perovskites with high n numbers (n \geq 3) is highly efficient. Therefore, high-performance opto-electronic devices, such as photo-detectors and sensors, can be developed using 2D perovskite single crystals with much improved environmental stabilities.

EXPERIMENTAL PROCEDURES

Resource availability

Lead contact

Further information and requests for resources should be directed to and will be fulfilled by the lead contact, Dr. Wanyi Nie (wanyi@lanl.gov).

Materials availability

This study did not generate new materials.

Perovskite single-crystal growth

3D MAPbl $_3$ single crystals are grown using the inverse temperature crystal growth method reported in the literature. ²⁶ Briefly, an equimolar ratio of methylammonium iodide (MAI) and lead iodide (Pbl $_2$) are dissolved in gamma butyrolactone (GBL) to obtain a 1 M solution and heat to 60°C. After completely dissolving the precursor solution, the solution is filtered with a 0.45 μ m PTFE filter, and the filtered solution is heated at 140°C for 1 h to obtain small MAPbl $_3$ crystals (<1 mm). The small crystals are placed in a fresh precursor solution as a seed and allowed to grow overnight to obtain large (\sim 1 cm) single crystals. 2D single crystals are grown using the inverse temperature crystal growth method reported in the literature. ^{24,25} Lead oxide (PbO), butylammonium iodide (BAI), and MAI with desired ratio are dissolved in hydriodic acid (57 wt % in H $_2$ O) and hypophosphorous acid (50 wt % in H $_2$ O) solution (ratio 5:1) and heated to 120°C with constant stirring for 1 h to obtain a clear yellow solution. PbO:MAI:BAI ratio for n = 1, n = 2, and n = 3 is 1:0:1, 2:1:1.4, and 3:2:1, respectively. The solution was slowly cooled at 1°C per h to room temperature to obtain 2D crystals.

Device fabrication

2 to 10 mm large and approximately 0.1 to 1 mm thick 2D bulk crystals are used. The surfaces of the 2D crystals are cleaved with scotch tape to obtain a fresh surface. A wire mask is used to define a lateral channel width of 160 μ m between a drain and a source metal electrode. E-beam deposition (Au) or thermal deposition (Pb) is used to deposit 100-nm-thick metal electrodes on the (001) surface of the crystals. Finally, the devices are brought into contact with silver paste.

Photoluminescence measurements

Photoluminescence spectra are recorded using a custom-built setup consisting of a 405-nm laser (Thor labs) and a 50 × objective lens with a numerical aperture of 0.50. PL spectra are measured using a spectrograph (Princeton Instruments, Pro EM 1024). Time-resolved PL measurements were performed using a 375 nm pulsed laser (LDH-D) with a pulse width of 40 ps and an average power of 0.5 mW at a repetition





frequency of 2.5 MHz. An avalanche photo-diode (MPD-SPAD) and a time-correlated single-photon counting module (Hydraharp 400) were used to measure the photon counts and obtain time-resolved PL. The measurements were taken at room temperature under ambient conditions.

SPCM

Devices are illuminated using a continuous 405 nm laser focused on the sample using a NA 0.5 50× objective lens. The diameter of the laser spot is approximately 1–2 μm , as determined by our camera. Neutral density filters are used to reduce the laser intensity to 50–200 W/cm². A mechanical chopper is used to modulate the light frequency at 20 Hz. Photocurrent is measured using a lock-in amplifier (SR830). A Keithley 2400 voltage source is used to apply bias. We always apply voltage bias on the source electrode and ground the drain electrode. Devices are mounted on a piezo-electric stage (Nano-Drive, MCL) and scanned with a step size of 1 μm from the source to drain. Photocurrent as a function of laser position is recorded to obtain a photocurrent line scan. A schematic of the experimental setup is shown in Figure 2A.

I-V characteristic

A Keithley 2400 is used to measure the dark and photocurrent. Devices are illuminated using a continuous 405 nm laser focused on the sample by a NA 0.5 50×10^{-2} objective lens. The diameter of the laser spot is approximately 1–2 μ m, as determined by our camera. Neutral density filters are used to reduce the laser intensity to 50–200 W/cm². For low temperature measurements, the samples are mounted on a cryostat (Linkam THMS350V), pumped to 1E-5 Torr pressure, and then cooled.

XPS and UPS characterizations

The X-ray photoelectron spectroscopy (XPS) and ultraviolet photoelectron spectroscopy (UPS) results were acquired using a PHI 5000 VersaProbe (ULVAC-PHI, Japan) system. During the XPS measurement, a monochromatic AI K α X-ray beam with a beam diameter of 100 μ m was applied to generate the characteristic photoelectrons. To compensate the surface charge, 10 V electron and 10 V Ar $^+$ flooding were applied during the data acquisition. For the UPS measurement, He I-line photons with a photon energy of 21.2 eV were generated using a discharge lamp and used as the ultraviolet radiation source. All the UPS spectra were recorded under a proper stage bias, and an Au film deposited on Si wafer was used as the reference sample to calibrate the Fermi level. The work-function of the investigated material was determined by subtracting the photon energy (21.2 eV) from the UPS cut-off energy. The valence-band maximum (VBM) position of the investigated surface was determined by subtracting the width of the acquired UPS spectrum (cut-off energy minus on-set energy) with a photon energy (21.2 eV).

SUPPLEMENTAL INFORMATION

Supplemental information can be found online at https://doi.org/10.1016/j.chempr. 2022.01.008.

ACKNOWLEDGMENTS

S.S. and W.N. acknowledge the mission foundation research project, as well as the exploratory research project support by the Laboratory Directed Research Directions program office (LDRD) at Los Alamos National Laboratory (LANL). H.T. acknowledges the financial support from the J. Robert Oppenheimer (JRO)





Distinguished Postdoc Fellowship at LANL. X.L. acknowledges support from the National Science Foundation DMR Program (award no. DMR-1905990). This work was performed, in part, at the Center for Integrated Nanotechnologies, an Office of Science User Facility operated for the U.S. Department of Energy (DOE) Office of Science by LANL (contract 89233218CNA000001). Use of the Center for Nanoscale Materials, an Office of Science User Facility, was supported by the U.S. Department of Energy, Office of Science, Office of Basic Energy Sciences under contract no. DE-AC02-06CH11357. L.W. and H.-H.H acknowledge the financial support from the Ministry of Science and Technology, Taiwan (MOST 108-2113-M-002-015-MY3 and 108-2911-I-002-561); Academia Sinica, Taiwan (AS-iMATE-109-31); and the Center of Atomic Initiative for New Materials, National Taiwan University.

AUTHOR CONTRIBUTIONS

W.N. conceived the project and organized the manuscript with S.S.; S.S. grew the crystals with H.T.; S.S. fabricated the devices and performed the SPCM and current-voltage measurements and analyzed the data with W.N.; X.L. and X.M. performed the TRPL measurements and analyzed the data; C.H. and H.H. performed the XPS and UPS characterizations and analyzed the data under the supervision of J.S. and L.W; and D.G. and S. T. interpreted the experimental data and helped with the discussion. All authors have contributed to the writing of the manuscript.

DECLARATION OF INTERESTS

The authors declare no competing interests.

Received: July 13, 2021 Revised: October 16, 2021 Accepted: January 14, 2022 Published: February 8, 2022

REFERENCES

- Saparov, B., and Mitzi, D.B. (2016). Organicinorganic perovskites: structural versatility for functional materials design. Chem. Rev. 116, 4558-4596.
- Gharibzadeh, S., Abdollahi Nejand, B., Jakoby, M., Abzieher, T., Hauschild, D., Moghadamzadeh, S., Schwenzer, J.A., Brenner, P., Schmager, R., Haghighirad, A.A., et al. (2019). Record open-circuit voltage widebandgap perovskite solar cells utilizing 2D/3D perovskite heterostructure. Adv. Energy Mater. 9, 1803699.
- Wang, Z., Lin, Q., Chmiel, F.P., Sakai, N., Herz, L.M., and Snaith, H.J. (2017). Efficient ambientair-stable solar cells with 2D–3D heterostructured butylammonium-caesiumformamidinium lead halide perovskites. Nat. Energy 2, 17135.
- Tsai, H., Nie, W., Blancon, J.C., Stoumpos, C.C., Asadpour, R., Harutyunyan, B., Neukirch, A.J., Verduzco, R., Crochet, J.J., Tretiak, S., et al. (2016). High-efficiency two-dimensional Ruddlesden-Popper perovskite solar cells. Nature 536, 312–316.
- Liu, F., Wang, L., Wang, J., Wang, F., Chen, Y., Zhang, S., Sun, H., Liu, J., Wang, G., Hu, Y., and Jiang, C. (2021). 2D Ruddlesden-Popper perovskite single crystal field-effect transistors. Adv. Funct. Mater. 31, 2005662.

- Zhang, Y., Liu, Y., Xu, Z., Yang, Z., and Liu, S.F. (2020). 2D perovskite single crystals with suppressed ion migration for highperformance planar-type photodetectors. Small 16, 2003145.
- Li, H., Song, J., Pan, W., Xu, D., Zhu, W.-A., Wei, H., and Yang, B. (2020). Sensitive and stable 2D perovskite single-crystal X-ray detectors enabled by a supramolecular anchor. Adv. Mater. 32, 2003790.
- Katan, C., Mercier, N., and Even, J. (2019). Quantum and dielectric confinement effects in lower-dimensional hybrid perovskite semiconductors. Chem. Rev. 119, 3140–3192.
- Pedesseau, L., Sapori, D., Traore, B., Robles, R., Fang, H.-H., Loi, M.A., Tsai, H., Nie, W., Blancon, J.-C., Neukirch, A., et al. (2016). Advances and promises of layered halide hybrid perovskite semiconductors. ACS Nano 10, 9776–9786.
- Blancon, J.C., Stier, A.V., Tsai, H., Nie, W., Stoumpos, C.C., Traoré, B., Pedesseau, L., Kepenekian, M., Katsutani, F., Noe, G.T., et al. (2018). Scaling law for excitons in 2D perovskite quantum wells. Nat. Commun. 9, 2254.
- 11. Tanaka, K., and Kondo, T. (2003). Bandgap and exciton binding energies in lead-iodide-based

- natural quantum-well crystals. Sci. Technol. Adv. Mater. 4, 599–604.
- Blancon, J.C., Tsai, H., Nie, W., Stoumpos, C.C., Pedesseau, L., Katan, C., Kepenekian, M., Soe, C.M.M., Appavoo, K., Sfeir, M.Y., et al. (2017). Extremely efficient internal exciton dissociation through edge states in layered 2D perovskites. Science 355, 1288–1292.
- Zhang, Z., Fang, W.-H., Long, R., and Prezhdo, O.V. (2019). Exciton dissociation and suppressed charge recombination at 2D perovskite edges: key roles of unsaturated halide bonds and thermal disorder. J. Am. Chem. Soc. 141, 15557–15566.
- Kinigstein, E.D., Tsai, H., Nie, W., Blancon, J.-C., Yager, K.G., Appavoo, K., Even, J., Kanatzidis, M.G., Mohite, A.D., and Sfeir, M.Y. (2020). Edge states drive exciton dissociation in Ruddlesden–Popper lead halide perovskite thin films. ACS Materials. Lett. 2, 1360–1367.
- Wang, K., Wu, C., Jiang, Y., Yang, D., Wang, K., and Priya, S. (2019). Distinct conducting layer edge states in two-dimensional (2D) halide perovskite. Sci. Adv. 5, eaau3241.
- Lu, J., Chen, W., Zhou, C., Yang, S., Wang, C., Wang, R., Wang, X., Gan, Z., Jia, B., and Wen, X. (2021). Layer number dependent exciton dissociation and carrier recombination in 2D





- Ruddlesden–Popper halide perovskites. J. Mater. Chem. C *9*, 8966–8974.
- Zhao, C., Tian, W., Sun, Q., Yin, Z., Leng, J., Wang, S., Liu, J., Wu, K., and Jin, S. (2020). Trapenabled long-distance carrier transport in perovskite quantum wells. J. Am. Chem. Soc. 142, 15091–15097.
- Seitz, M., Meléndez, M., Alcázar-Cano, N., Congreve, D.N., Delgado-Buscalioni, R., and Prins, F. (2021). Mapping the trap-state landscape in 2D metal-halide perovskites using transient photoluminescence microscopy. Adv. Optical Mater. 9, 2001875.
- Zhang, J., and Hu, B. (2021). Slow hot-carrier cooling enabled by uniformly arranging different-n-value nanoplates in Quasi-2D perovskites through long-range orbit-orbit interaction toward enhancing photovoltaic actions. J. Phys. Chem. Lett. 12, 4072–4078.
- Seitz, M., Magdaleno, A.J., Alcázar-Cano, N., Meléndez, M., Lubbers, T.J., Walraven, S.W., Pakdel, S., Prada, E., Delgado-Buscalioni, R., and Prins, F. (2020). Exciton diffusion in twodimensional metal-halide perovskites. Nat. Commun. 11, 2035.
- Zhou, C., Chen, W., Yang, S., Ou, Q., Gan, Z., Bao, Q., Jia, B., and Wen, X. (2020).
 Determining in-plane carrier diffusion in twodimensional perovskite using local timeresolved photoluminescence. ACS Appl. Mater. Interfaces 12, 26384–26390.
- Xiao, X., Wu, M., Ni, Z., Xu, S., Chen, S., Hu, J., Rudd, P.N., You, W., and Huang, J. (2020). Ultrafast exciton transport with a long diffusion length in layered perovskites with organic cation functionalization. Adv. Mater. 32, e2004080.
- 23. Deng, S., Shi, E., Yuan, L., Jin, L., Dou, L., and Huang, L. (2020). Long-range exciton transport and slow annihilation in two-dimensional hybrid perovskites. Nat. Commun. 11, 664.
- 24. Stoumpos, C.C., Cao, D.H., Clark, D.J., Young, J., Rondinelli, J.M., Jang, J.I., Hupp, J.T., and Kanatzidis, M.G. (2016). Ruddlesden-Popper hybrid lead iodide perovskite 2D homologous semiconductors. Chem. Mater. 28, 2852–2867.
- Leng, K., Abdelwahab, I., Verzhbitskiy, I., Telychko, M., Chu, L., Fu, W., Chi, X., Guo, N., Chen, Z., Chen, Z., et al. (2018). Molecularly thin two-dimensional hybrid perovskites with tunable optoelectronic properties due to reversible surface relaxation. Nat. Mater. 17, 908–914.
- 26. Liu, Y., Yang, Z., Cui, D., Ren, X., Sun, J., Liu, X., Zhang, J., Wei, Q., Fan, H., Yu, F., et al. (2015).

- Two-inch-sized perovskite CH3 NH3 PbX3 (X = Cl, Br, I) crystals: growth and characterization. Adv. Mater. 27, 5176–5183.
- Shrestha, S., Tsai, H., Yoho, M., Ghosh, D., Liu, F., Lei, Y., Tisdale, J., Baldwin, J., Xu, S., Neukirch, A.J., et al. (2020). Role of the metalsemiconductor interface in halide perovskite devices for radiation photon counting. ACS Appl. Mater. Interfaces 12, 45533–45540.
- 28. McClintock, L., Xiao, R., Hou, Y., Gibson, C., Travaglini, H.C., Abramovitch, D., Tan, L.Z., Senger, R.T., Fu, Y., Jin, S., and Yu, D. (2020). Temperature and gate dependence of carrier diffusion in single crystal methylammonium lead iodide perovskite microstructures. J. Phys. Chem. Lett. 11, 1000–1006.
- Howell, S.L., Jariwala, D., Wu, C.C., Chen, K.S., Sangwan, V.K., Kang, J., Marks, T.J., Hersam, M.C., and Lauhon, L.J. (2015). Investigation of band-offsets at monolayer-multilayer MoS(2) junctions by scanning photocurrent microscopy. Nano Lett 15, 2278–2284.
- 30. Nanot, S., Cummings, A.W., Pint, C.L., Ikeuchi, A., Akiho, T., Sueoka, K., Hauge, R.H., Léonard, F., and Kono, J. (2013). Broadband, polarization-sensitive photodetector based on optically-thick films of macroscopically long, dense, and aligned carbon nanotubes. Sci. Rep. 3, 1335.
- Strasfeld, D.B., Dorn, A., Wanger, D.D., and Bawendi, M.G. (2012). Imaging Schottky barriers and ohmic contacts in PbS quantum dot devices. Nano Lett 12, 569–575.
- Graham, R., and Yu, D. (2013). Scanning photocurrent microscopy in semiconductor nanostructures. Mod. Phys. Lett. B 27.
- 33. Liu, S., Wang, L., Lin, W.C., Sucharitakul, S., Burda, C., and Gao, X.P. (2016). Imaging the long transport lengths of photo-generated carriers in oriented perovskite films. Nano Lett 16, 7925–7929.
- Baranowski, M., and Plochocka, P. (2020). Excitons in metal-halide perovskites. Adv. Energy Mater. 10.
- 35. Spitha, N., Kohler, D.D., Hautzinger, M.P., Li, J., Jin, S., and Wright, J.C. (2020). Discerning between exciton and free-carrier behaviors in Ruddlesden-Popper perovskite quantum wells through kinetic modeling of photoluminescence dynamics. J. Phys. Chem. C 124, 17430–17439.
- 36. Hou, Y., Wang, R., Xiao, R., McClintock, L., Clark Travaglini, H., Paulus Francia, J., Fetsch, H., Erten, O., Savrasov, S.Y., Wang, B., et al. (2019). Millimetre-long transport of

- photogenerated carriers in topological insulators. Nat. Commun. 10, 5723.
- 37. Wen, X., Feng, Y., Huang, S., Huang, F., Cheng, Y.-B., Green, M., and Ho-Baillie, A. (2016). Defect trapping states and charge carrier recombination in organic–inorganic halide perovskites. J. Mater. Chem. C 4, 793–800.
- Du, T., Kim, J., Ngiam, J., Xu, S., Barnes, P.R.F., Durrant, J.R., and McLachlan, M.A. (2018). Elucidating the origins of subgap tail states and open-circuit voltage in methylammonium lead triiodide perovskite solar cells. Adv. Funct. Mater. 28.
- Peng, W., Yin, J., Ho, K.T., Ouellette, O., De Bastiani, M., Murali, B., El Tall, O., Shen, C., Miao, X., Pan, J., et al. (2017). Ultralow selfdoping in two-dimensional hybrid perovskite single crystals. Nano Lett 17, 4759–4767.
- Wang, Y., Tang, Y., Jiang, J., Zhang, Q., Sun, J., Hu, Y., Cui, Q., Teng, F., Lou, Z., and Hou, Y. (2020). Mixed-dimensional self-assembly organic-inorganic perovskite microcrystals for stable and efficient photodetectors. J. Mater. Chem. C 8, 5399–5408.
- Kepenekian, M., Traore, B., Blancon, J.C., Pedesseau, L., Tsai, H., Nie, W., Stoumpos, C.C., Kanatzidis, M.G., Even, J., Mohite, A.D., et al. (2018). Concept of lattice mismatch and emergence of surface states in twodimensional hybrid perovskite quantum wells. Nano Lett 18, 5603–5609.
- Qin, Z., Dai, S., Gajjela, C.C., Wang, C., Hadjiev, V.G., Yang, G., Li, J., Zhong, X., Tang, Z., Yao, Y., et al. (2020). Spontaneous formation of 2D/ 3D heterostructures on the edges of 2D Ruddlesden–Popper hybrid perovskite crystals. Chem. Mater. 32, 5009–5015.
- Sridharan, A., Noel, N.K., Rand, B.P., and Kéna-Cohen, S. (2021). Role of photon recycling and band filling in halide perovskite photoluminescence under focussed excitation conditions. J. Phys. Chem. C 125, 2240–2249.
- Staub, F., Anusca, I., Lupascu, D.C., Rau, U., and Kirchartz, T. (2020). Effect of reabsorption and photon recycling on photoluminescence spectra and transients in lead-halide perovskite crystals. J. Phys. Mater. 3, 025003.
- Fang, Y., Wei, H., Dong, Q., and Huang, J. (2017). Quantification of re-absorption and reemission processes to determine photon recycling efficiency in perovskite single crystals. Nat. Commun. 8, 14417.